Annals of Nuclear Energy 183 (2023) 109651

Contents lists available at ScienceDirect

Annals of Nuclear Energy

journal homepage: www.elsevier.com/locate/anucene

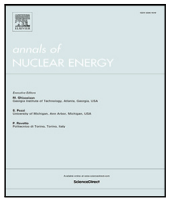

Total thermal neutron cross section measurements of hydrogen dense polymers from 0.0005–20 eV

D. Fritz [a,*], Y. Danon [a], K. Ramic [d], C.W. Chapman [d], J.M. Brown [d], G. Arbanas [d], M. Rapp [b], T.H. Trumbull [b], M. Zerkle [c], J. Holmes [c], P. Brain [a], A. Ney [a], S. Singh [a], K. Cook [a], B. Wang [a]

[a] Gaerttner LINAC Center, Rensselaer Polytechnic Institute, Troy, NY 12180, USA
[b] Naval Nuclear Laboratory, P.O. Box 1072, Schenectady, NY 12301, USA
[c] Naval Nuclear Laboratory, PO Box 79, West Mifflin, PA 15122, USA
[d] Nuclear Energy and Fuel Cycle Division, Oak Ridge National Laboratory, Oak Ridge, TN 37830, USA

ARTICLE INFO

Keywords:
Polyethylene
Polystyrene
Plexiglas
Total cross section
Thermal scattering law

ABSTRACT

Hydrogen dense polymers, specifically polyethylene, polystyrene, and Plexiglas, have served as neutron moderator and reflector materials in hundreds of separate critical benchmark experiments because of their low cost and abundance of hydrogen. In order to accurately model and simulate these critical benchmarks, the thermal scattering law (TSL) evaluation that governs how neutrons will thermalize must be well understood and rigorously validated. To support this validation, researchers at Rensselaer Polytechnic Institute performed total neutron cross section measurements for high-density polyethylene & polystyrene over the energy range 0.0005–20 eV and for Plexiglas G & Plexiglas G-UVT over the energy range 0.0005–3 eV. Comparisons were made between the measured cross section and that predicted by the ENDF/B-VIII.0 and Oak Ridge National Laboratory/European Spallation Source/Rensselaer Polytechnic Institute TSL evaluations for polyethylene, Plexiglas, and polystyrene, as available. These experiments represent the first total neutron cross section measurements for polystyrene.

1. Introduction

Hydrogen dense materials are typically ideal moderator and reflector materials due to the high cross section of hydrogen and its strong ability to down-scatter neutrons. To this end, hydrocarbons provide an inexpensive and solid phase hydrogen dense alternative to water that is easy and effective to use in compact spaces. As a consequence of these favorable qualities, hydrocarbon materials have seen extensive use in critical benchmarks. Hundreds of separate critical benchmark configurations have employed polyethylene, polystyrene or Plexiglas as a moderator and/or a reflector material (Bess et al., 2019). Due to this substantial use, rigorous validation of the polyethylene, polystyrene and Plexiglas thermal scattering law evaluations is required.

In order to accurately model the performance of hydrocarbons for any nuclear system, the scattering interactions between neutrons and the hydrocarbon molecules must be well understood. More specifically, the impact of the molecular bonds of the hydrocarbon on neutron scattering interactions must be accounted for below a neutron energy of 3 eV. The effects of these molecular bonds are accounted for in transport codes, such as MCNP (Werner et al., 2018), through the use of thermal scattering law (TSL) evaluations.

Phonon spectra serve as the basis for TSL evaluations since they represent the various molecular motions of a material. In order to generate a thermal scattering kernel for use in MCNP, $S(\alpha,\beta)$ calculations are performed with these phonon spectra in codes such as NJOY (Macfarlane et al., 2017), FLASSH (Zhu and Hawari, 2018) and oClimax (Cheng and Ramirez-Cuesta, 2020). As with any calculated value, these thermal scattering kernels generated from TSL evaluations require experimental validation, especially since thermal scattering can have a large impact on system criticality. The most important form of experimental validation for thermal scattering kernels comes in the form of total cross section measurements. This report details high accuracy measurements performed for polyethylene, polystyrene, Plexiglas G and Plexiglas G-UVT. Comparisons are made to the ENDF/B-VIII.0 (Brown et al., 2018) and Oak Ridge National Laboratory (ORNL)/European Spallation Source (ESS)/Rensselaer Polytechnic Institute (RPI) TSL evaluations for polyethylene, Plexiglas (Lucite) and polystyrene, as applicable (Ramic et al., 2018, 2019).

* Corresponding author.
E-mail address: fritzd3@rpi.edu (D. Fritz).

https://doi.org/10.1016/j.anucene.2022.109651
Received 12 August 2022; Received in revised form 11 December 2022; Accepted 12 December 2022
Available online 27 December 2022

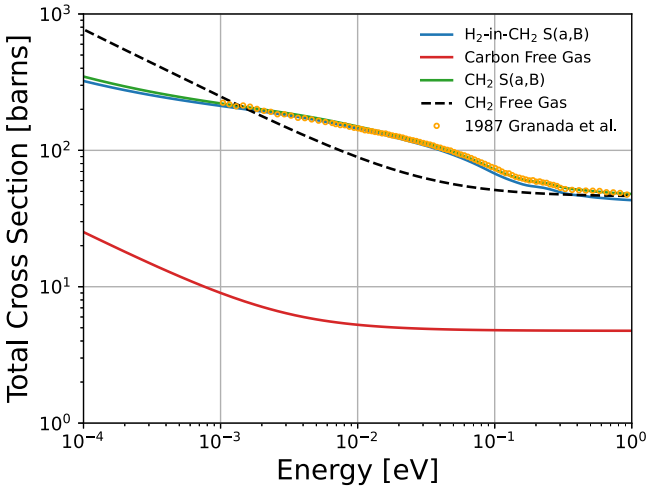

Fig. 1. ENDF/B-VIII.0 $S(\alpha, \beta)$ and free gas total cross section compared with experimental data for polyethylene.

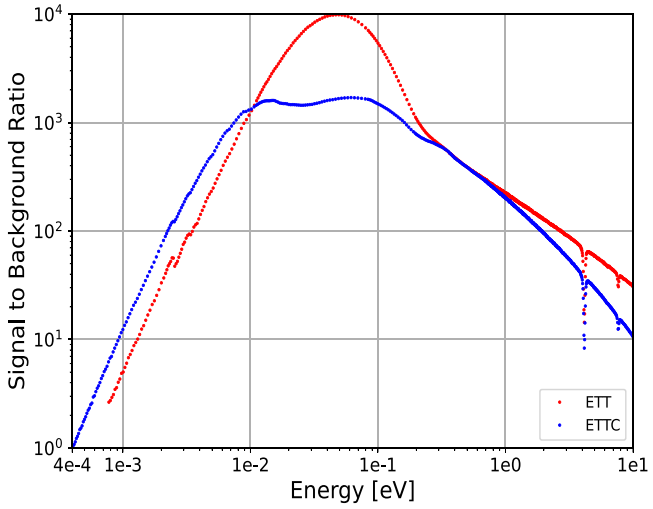

Fig. 2. Signal to background ratio for ETT and ETTC targets. The structure present at high and low energies are due to resonances from a tungsten fixed notch and Bragg edges from in-beam lead, respectively.

2. Overview of polymers

While polyethylene $[(C_2H_4)_n]$, polystyrene $[(C_8H_8)_n]$ and Plexiglas $[(C_5O_2H_8)_n]$ have different chemical formulas, their neutron cross section is dominated by the cross section of hydrogen. Their large carbon components also play a significant role in the total bound cross section, but the molecular bond effect for the molecule is overwhelmingly dominated by the hydrogen component. Therefore, it is often found that only the hydrogen component is necessary in thermal scattering law evaluations, such as in ENDF/B-VIII.0. For the purpose of this report, only the impact of the hydrogen component in ENDF/B-VIII.0 TSL evaluations is compared against experimental data. However, the impact of all components present in the ORNL/ESS/RPI TSL evaluation for polyethylene (hydrogen, carbon) and the ORNL/RPI TSL evaluations for polystyrene (hydrogen, carbon) and Plexiglas (hydrogen, carbon, oxygen) were compared against experimental data.

Polyethylene (specifically high density polyethylene) is the most well understood of the three polymers, with both ENDF/B-VIII.0 and ORNL/ESS/RPI TSL evaluations, as well as several total cross section measurements available. The thermal scattering law evaluation and free gas model are compared for polyethylene total cross section (XS) in Fig. 1 below, where the hydrogen and carbon components (per atom) are highlighted. The dominance of the hydrogen cross section over the carbon cross section is easy to see in Fig. 1. Below 1 eV there is a rapid divergence in the total cross section for polyethylene due to the molecular bond effect from the hydrogen component. With the inclusion of total cross section data from Granada et al. (1987), the TSL evaluation clearly predicts the total cross section of polyethylene much more accurately than the free gas model.

While ENDF/B-VIII.0 and ORNL/RPI TSL evaluations and some experimental data do exist for Plexiglas, there are many different types and the evaluations/experiments do not differentiate between the types of Plexiglas. For polystyrene, only a preliminary ORNL/RPI TSL evaluation exists, with no measured total thermal cross sections in existence as would be required for validation. It should be noted that the hydrogen density of both Plexiglas and polystyrene is lower than that of polyethylene.

3. Experimental methods and materials

In order to validate thermal scattering law evaluations for the various polymer materials, total thermal neutron cross section measurements were performed. For the polyethylene and polystyrene measurements, two different neutron production targets were used: the enhanced thermal target (ETT) and the enhanced thermal target + cold moderator (ETTC). The ETT target is suitable for measurements from 0.001–20 eV, while the ETTC is intended for measurements from 0.0005–3 eV. For the Plexiglas measurements, only the ETTC target was used. The signal to background ratios for these two target as they were configured for these measurements are shown in Fig. 2. It should be noted that at energies below 0.02 eV, the ETTC produces up to 8 times as much signal as the ETT after background subtraction (Fritz and Danon, 2022).

Table 1
Beam conditions and in-beam components.

Parameter	ETT	ETTC
Average electron current [μA]	5.6	4.9
Average electron energy [MeV]	48.5	45.5
Repetition rate [Hz]	25	18
Pulse width [ns]	500	628
Number of bins	96,512	135,040
Bin width [ns]	409.6	409.6
Flight path [m]	14.973	14.927
Component	**ETT**	**ETTC**
Additional in-beam lead [in]	1/4	3/8
Shadow shield	Used	Not Used
He gas [m]	3	3
Mylar windows [in]	0.025	0.025
Aluminum windows [in]	0.03	0.03

The structure present in the signal to background ratios at low energies is from in-beam lead, while at high energies resonances from an in-beam fixed tungsten notch filter are visible. For more information concerning these targets, please see Fritz and Danon (2021). A 3 mm thick (GS-20) lithium glass detector was placed 15 meters away from each configuration. The data from this detector flows to a time of flight (TOF) clock via a pre-amplifier, amplifier, constant fraction discriminator and level adapter. A data acquisition computer controls and reads the TOF clock and allows for autonomous data collection above 20 eV for this flight path. The parameters of the LINAC and the in-beam components utilized for each experimental configuration are listed below in Table 1. The shadow shield mentioned in Table 1 refers to an 8" long lead block placed in front of the neutron production target to reduce background from photons.

For the purpose of effectively measuring cross section for each polymer material, two sample thicknesses were chosen for each material. In the case of the Plexiglas material, two slightly different types of Plexiglas were selected. The physical dimensions and mass of each sample

Table 2
Polyethylene and polystyrene sample dimensions.

Sample & thickness [in]	Length [cm]	Width [cm]	Mass [g]	Atomic areal density [atom/barn]
Polyethylene, 3/32	12.748 ± 0.014	12.748 ± 0.030	37.0882 ± 0.0007	0.00980 ± 0.00003
Polyethylene, 1/16	12.741 ± 0.005	12.736 ± 0.019	24.0947 ± 0.0002	0.00638 ± 0.00001
Polystyrene, 5/32	12.670 ± 0.010	12.657 ± 0.032	61.3445 ± 0.0006	0.01770 ± 0.00005
Polystyrene, 3/32	12.667 ± 0.023	12.662 ± 0.013	37.5789 ± 0.0004	0.01084 ± 0.00002

Table 3
Plexiglas sample dimensions.

Sample & thickness [in]	Diameter [cm]	Mass [g]	Atomic areal density [atom/barn]
Plexiglas G-UVT, 0.184	4.869 ± 0.001	10.3421 ± 0.0001	0.003340 ± 0.000001
Plexiglas G, 0.121	4.879 ± 0.001	6.7688 ± 0.0001	0.002178 ± 0.000001

Table 4
Sample impurity analysis.

Sample	Polyethylene	Polystyrene	Plexiglas G	Plexiglas G-UVT
Element	Conc.	Conc.	Conc.	Conc.
Boron	<20 ppm	<20 ppm	<20 ppm	<20 ppm
Cadmium	<2 ppm	<2 ppm	<2 ppm	<2 ppm
Gadolinium	<2 ppm	<2 ppm	<2 ppm	<2 ppm

were measured to calculate the areal density used in the calculation of cross section, as shown through Eq. (1), assuming material uniformity. The dimensions for each sample, and their associated uncertainty, are displayed below in Tables 2 and 3. The atomic masses of carbon and hydrogen were combined to form a molar mass of 14.02665 g/mol and 13.01883 g/mol for polyethylene (simplified to CH_2) and polystyrene (simplified to CH), respectively. For Plexiglas, the atomic mass of oxygen was combined with carbon and hydrogen to form a molar mass of 100.11566 g/mol. An atomic mass of 1.007825, 12.011 and 15.99903 [g/mol] were used for hydrogen, carbon and oxygen, respectively de Laeter et al. (2003).

$$N = \frac{m * N_a}{M * A} \tag{1}$$

Where:

N: Atomic areal density.

m, A: Sample mass and area.

N_a: Avogadro's number.

M: Molar Mass.

In the case of the polyethylene and polystyrene samples, large square sheets of uniform thickness were used. For the two Plexiglas samples, a cylindrical sample was used. It can be seen that for all samples, the uncertainty on the areal density is less than 0.3%. Prior to experimentation, a broad spectrum elemental impurity analysis was performed for each material for a wide variety of elements ranging from lithium to uranium, with the overwhelming majority of elements having a concentration below 2 ppm, or the typical minimum detectable limit. The concentrations of boron, cadmium and gadolinium are displayed below in Table 4 and were all below the minimum detectable limit for the analysis performed.

4. Calculation of cross section and associated uncertainty

4.1. Cross section

In order to determine the total cross section of a sample, two quantities are measured: the detector count rate with the sample in the beam and the detector count rate with the sample out of the beam, also referred to as open. The ETTC measured signal and background count rates for the open and polyethylene 3/32" sample are shown in Fig. 3 below. Here it can be seen that the background rate for the polyethylene 3/32" sample is well below the polyethylene 3/32" sample signal rate until about 0.001 eV, where the signal count rate spectrum

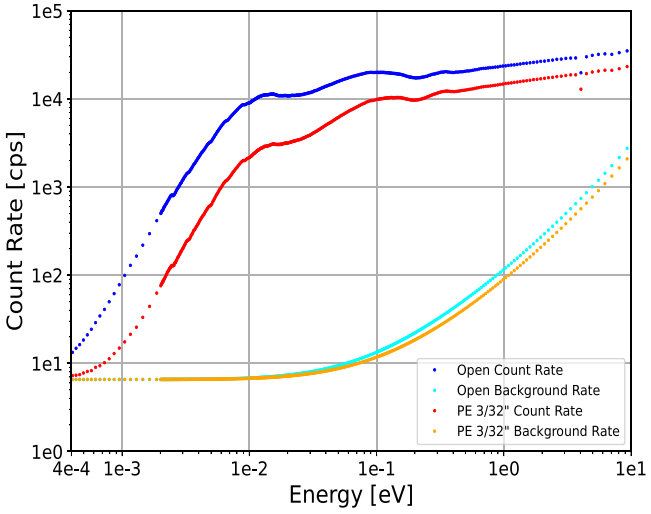

Fig. 3. ETTC signal and background count rates for the open and the 3/32" polyethylene sample.

begins to curve. This curving occurs from the low signal-to-background ratio at and below this energy for the polyethylene 3/32" sample. By contrast, the open observed a higher signal-to-background ratio than the polyethylene sample and thus does not experience curving in its spectrum until 0.0004 eV. It should be noted that the open and polyethylene 3/32" sample signal rates shown in Fig. 3 are not background subtracted. The structure present in both signal rates at low energy are Bragg edges from the in-beam lead, while the dip around 4 eV is due to a resonance from the in-beam tungsten fixed notch filter. The effects of both the lead Bragg edges and the tungsten resonance are washed out in transmission since the same amount of lead and tungsten was present in all measured samples.

For each sample, the count rate is dead-time corrected and normalized using beam-intensity monitors, then background subtracted. To find the transmission for each TOF channel, $T(t_i)$, the count rate in the sample, $C_S(t_i)$, must be divided by the count rate in the open, $C_O(t_i)$, as shown in Eq. (2) (Danon, 1993).

$$T(t_i) = \frac{(C_s(t_i) - K_s B(t_i) - B0_s)}{(C_o(t_i) - K_o B(t_i) - B0_o)} \tag{2}$$

Where

$B(t_i)$ [cps]: Fitted time-dependent background.

$B0_s$, $B0_o$ [cps]: Constant background in sample and open.

K_s, K_o: Time-dependent background normalization factors for sample and open.

When performing a transmission measurement, both the constant background, B0, and the time-dependent background, $B(t_i)$, must be considered for each sample. The constant background comes from many sources and is present for each TOF channel. The time-dependent

background varies for each TOF channel and stems from off-time neutrons and neutron leakage in the collimation system. A time-dependent background shape and normalization factors were determined for each sample by utilizing the double-notch (black resonance) method (Syme, 1982) with indium and cadmium notch filters in dedicated background runs. A silver notch filter was also used for the polyethylene and polystyrene samples, but not for the Plexiglas samples. To characterize the constant background the double-notch method was applied at the very end of the TOF data collection in the background runs for each sample.

Once the transmission for a sample has been measured and all necessary background subtraction performed, the total cross section, $\sigma_{t,measured}(t_i)$, was then calculated through Eq. (3) below.

$$\sigma_{t,measured}(t_i) = \frac{-1}{N} * ln(T(t_i)) \text{ [barns]} \tag{3}$$

Where

N [atom/barns]: Atomic areal density.

In order to relate a neutron's time of arrival, t [μs], to its non-relativistic energy, E [eV], Eq. (4) was used for each TOF channel. However, when converting from time of arrival to energy, the measured time needs to be corrected for the flight time of the electron pulse to the target, t0 [μs], due to the TOF clock starting at the birth of the electron pulse. This t0 values represents the delay before the creation of the neutron burst and was assessed to be 3.072 μs for all samples by measuring the gamma flash arrival time to the detector. The gamma flash coincides with the arrival time of the electron pulse to the target, corrected for the flight time of the photons.

$$E = \left(\frac{K\,L}{t - t0}\right)^2 \text{ [eV]} \tag{4}$$

Where

L [m]: Flight path length (see Table 1).

K: 72.29824 $\left[\frac{\sqrt{\text{eV}}\mu\text{s}}{\text{m}}\right]$.

4.2. Associated uncertainty

In the case of transmission measurements, the overall uncertainty can be broken down into statistical and non-statistical components. The statistical uncertainty component arises from counting statistics applied to the thermal neutron detector and monitor detector system for sample counts and normalizing sample counts to beam intensity, respectfully. Non-statistical uncertainty is a much broader component, but is primarily attributed to how well the monitor detector system tracks variations in the beam intensity seen by the thermal neutron detector throughout the experiment. For the various polymer samples, the monitor tracking uncertainty contributed approximately 0.75%–1.2% to the total uncertainty in transmission.

Eq. (5) below indicates how the statistical uncertainty in the transmission for a given sample, $\Delta T_{stat}(t_i)$, is found through the propagation of all sources of statistical uncertainty, assuming the sources are independent (Danon, 1993).

$$\left(\frac{\Delta T_{stat}(t_i)}{T(t_i)}\right)^2 = \left(\frac{\Delta C_s(t_i)}{R_s(t_i)}\right)^2 + \left(\frac{\Delta C_o(t_i)}{R_o(t_i)}\right)^2 + \left(\frac{\Delta B0_s}{R_s(t_i)}\right)^2 + \left(\frac{\Delta B0_o}{R_o(t_i)}\right)^2 + \left(\frac{K_o}{R_o(t_i)} - \frac{K_s}{R_s(t_i)}\right)^2 \Delta B(t_i)^2 \tag{5}$$

Where

$R_s(t_i)$ [cps] $= C_s(t_i) - K_s B(t_i) - B0_s$

$R_o(t_i)$ [cps] $= C_o(t_i) - K_o B(t_i) - B0_o$

$\Delta C_o(t_i)$, $\Delta C_s(t_i)$: Uncertainty in open, sample count rate.

$\Delta B0_o$, $\Delta B0_s$: Uncertainty in open, sample constant background.

$\Delta B(t_i)$: Uncertainty in time-dependent background.

Eq. (2) was then modified to include monitor normalization factors in order to accurately account for non-statistical sources of uncertainty, shown in Eq. (6) below. It is important to note that the normalization factors shown in Eq. (6) are all equal to 1, but their associated uncertainty is propagated to the overall uncertainty of transmission.

$$T(t_i) = \frac{F_s(C_s(t_i) - B0_s) - F_B K_s B(t_i)}{F_o(C_o(t_i) - B0_o) - F_B K_o B(t_i)} \tag{6}$$

Where

F_s: Monitor normalization factor for sample.

F_o: Monitor normalization factor for open.

F_B: Monitor normalization factor for time-dependent background.

Since the same monitor detector system was used to determine each of the normalization factors in Eq. (6), the correlations between these factors, and other variables in the transmission equation, needed to be accounted for. The derivative of transmission with respect to each statistical (sample and open count rate) and systematic (all other variables) variable in Eq. (6) was calculated. These derivatives and their associated uncertainties were used to form separate covariance matrices for the statistical and systematic variables. During the creation of the systematic variable covariance matrix, the covariance matrix from the time-dependent background fitting was included. The covariance matrix for the systematic variables was then added to the covariance matrix for the statistical variables to form a final covariance matrix that includes all quantifiable sources of uncertainty. For more information concerning the creation of this final covariance matrix, see the discussion of uncertainty and correlation in Brown (2019).

Fig. 4 below shows the correlation matrix for transmission of the Plexiglas G 0.121" sample from 0.0005–3 eV. The correlation matrix indicates high levels of correlation between energies except at very low energies, where the relative contribution from statistical uncertainty increases significantly. The strong correlation between energies arises from the very large contribution by the monitor tracking uncertainty to the total transmission uncertainty. Without the inclusion of the monitor tracking uncertainty, little to no correlation is seen in the off diagonal.

The values of the covariance matrix diagonal for transmission were then propagated to cross section uncertainty. Eq. (7) shows how the uncertainty in the measured total cross section was found by combining the uncertainties from both transmission, $\Delta T(t_i)$, and areal density, ΔN. Overall, the inclusion of systematic sources of uncertainty increases the total uncertainty in transmission over that calculated from Eq. (5) alone.

$$\left(\frac{\Delta\sigma_{t,measured}(t_i)}{\sigma_{t,measured}(t_i)}\right)^2 = \left(\frac{\Delta N}{N}\right)^2 + \left(\frac{\Delta T(t_i)}{T(t_i)}\right)^2 \left(\frac{1}{ln(T(t_i))}\right)^2 \tag{7}$$

5. Results and discussion

Once the background for each sample was characterized, the measured transmission was corrected and converted into cross section. Fig. 5 below shows a comparison of the total cross section (XS) of high-density polyethylene (PE) with the current ENDF/B-VIII.0 TSL evaluation, the ORNL/ESS/RPI TSL evaluation, as well as experimental data from Granada et al. (1987) and Lee et al. (2019). In general, good agreement is seen overall between the measured cross section, the ENDF/B-VIII.0 evaluation, the ORNL/ESS/RPI evaluation and the Granada/Lee data. Additionally, excellent agreement is seen between the four RPI polyethylene measurements over all energies. It should be noted that experimental error bars are plotted for the two PE 3/32" measurements and represent the diagonal of the calculated covariance matrix. All experimental data shown for all RPI polymer materials has an uncertainty less than 5%. Unless otherwise stated, all TSL evaluations shown were processed using NJOY.

Between 0.0005 and 0.05 eV some disagreement is seen between the ENDF/B-VIII.0 evaluation, the ORNL/ESS/RPI evaluation and all measured cross section from RPI, Granada and Lee, as shown in Fig. 6. Here the ENDF/B-VIII.0 evaluation is systematically higher than all measured cross section by a few percent from 0.003–0.05 eV. The ORNL/ESS/RPI evaluation is systematically higher than all measured

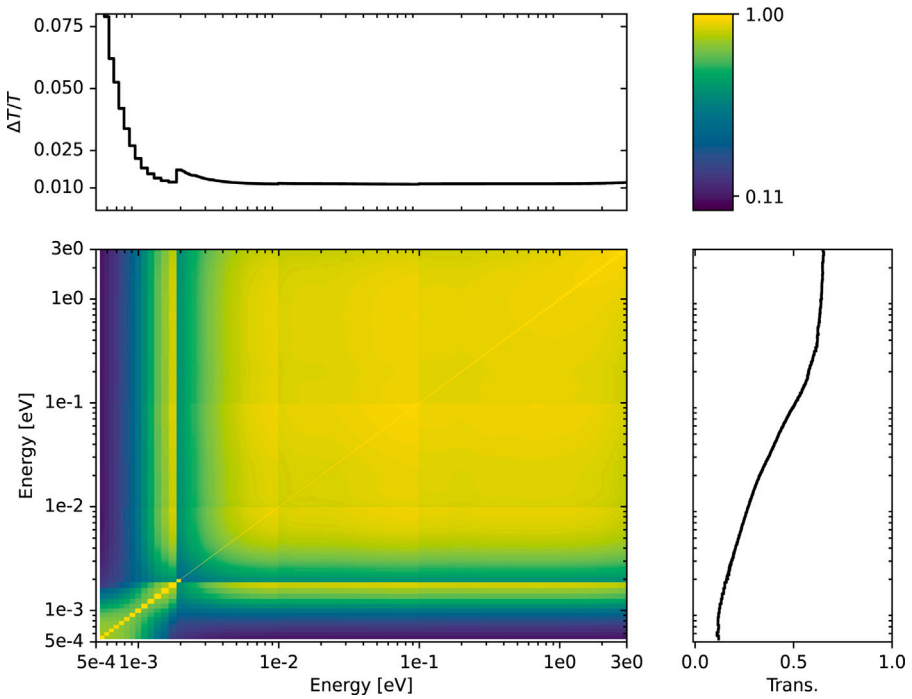

Fig. 4. Correlation matrix for Plexiglas G 0.121" sample from 0.0005–3 eV. Sudden changes in the transmission uncertainty are caused by time compression points.

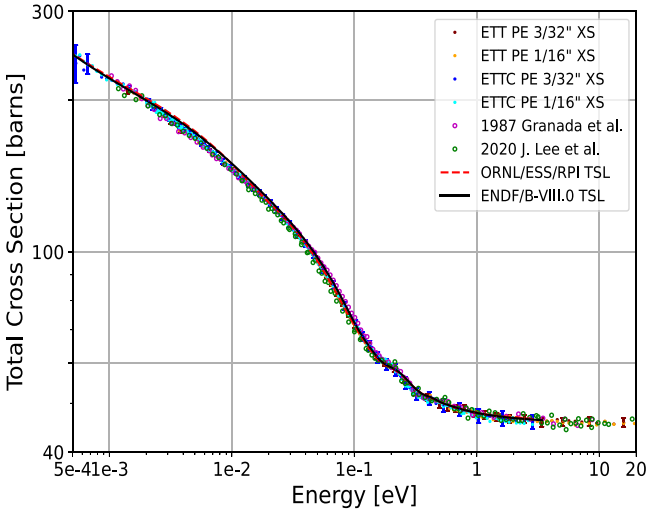

Fig. 5. Total cross section of high-density polyethylene from 0.0005–20 eV.

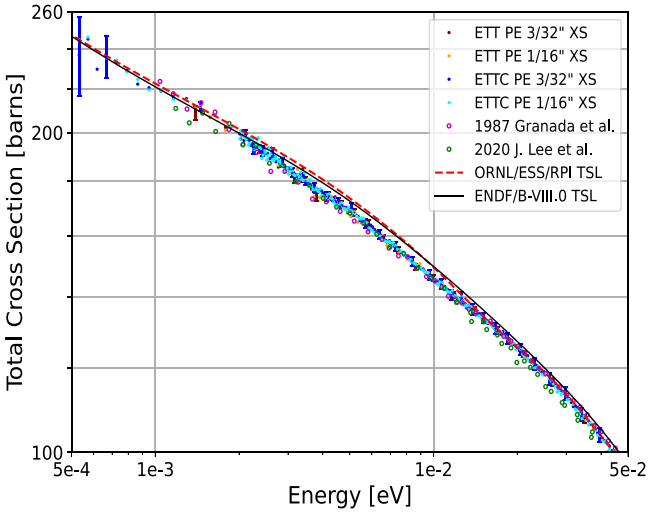

Fig. 6. Total cross section of high-density polyethylene from 0.0005–0.05 eV.

cross section from 0.002–0.015 eV. Additionally, the measured cross section of polyethylene has been extended below 0.001 eV by the RPI ETTC measurements.

At higher energies disagreement is found between the measured cross section from RPI and that from Granada/Lee, displayed below in Fig. 7. Between 0.015 and 0.15 eV, disagreement is seen between the Granada and Lee data, with all of the RPI measured cross section falling between the two. Above 0.15 eV a fluctuation occurs in the cross section, with the data from Granada/Lee agreeing with the RPI measured cross section. However, both the ENDF/B-VIII.0 evaluation and ORNL/ESS/RPI evaluation cross section fluctuations are slightly misaligned with the measured cross section fluctuation.

Due to the excellent agreement between the four RPI measurements for polyethylene, the cross section averaging method found in Danon et al. (2009) could be applied. This average cross section was then used to create a C/E plot to more thoroughly highlight the differences between the RPI experimental data and the TSL evaluations for polyethylene, shown in Fig. 8. For energies below 0.01 eV and above 0.2 eV the ENDF/B-VIII.0 and ORNL/ESS/RPI TSL evaluations have similar comparisons to the average RPI polyethylene cross section. However, from 0.01–0.1 eV the ORNL/ESS/RPI TSL evaluation shows better agreement with the RPI experimental data than the ENDF/B-VIII.0 TSL evaluation.

In order to probe the differences between the ENDF/B-VIII.0 and ORNL/ESS/RPI TSL evaluations for polyethylene further, these evaluations were compared at energies down to 0.1 μeV in Fig. 9, where ultracold experimental data from Pokotilovski et al. (2011) was added. Below 0.001 eV, a noticeable divergence in the total cross section occurs between the two TSL evaluations. From 0.1–2 μeV, the ORNL/ESS/RPI TSL evaluation agrees better with the Pokotilovski measurement at these energies. Both of the TSL evaluations were processed with NCrystal (Cai and Kittlemann, 2020) in Fig. 9 due to energy grid limitations

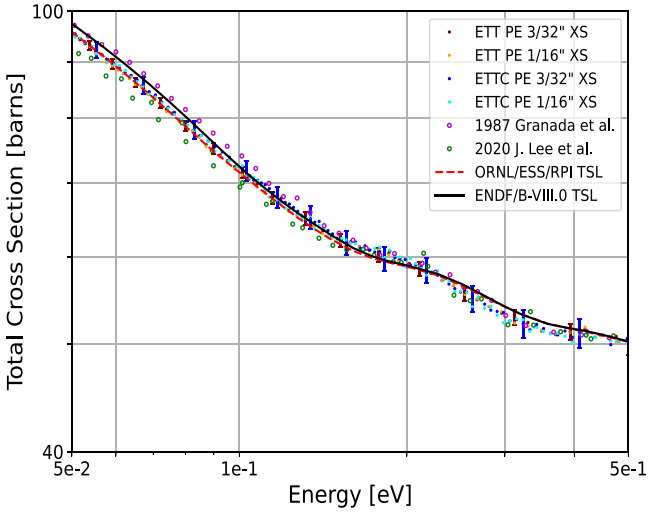

Fig. 7. Total cross section of high-density polyethylene from 0.05–0.5 eV.

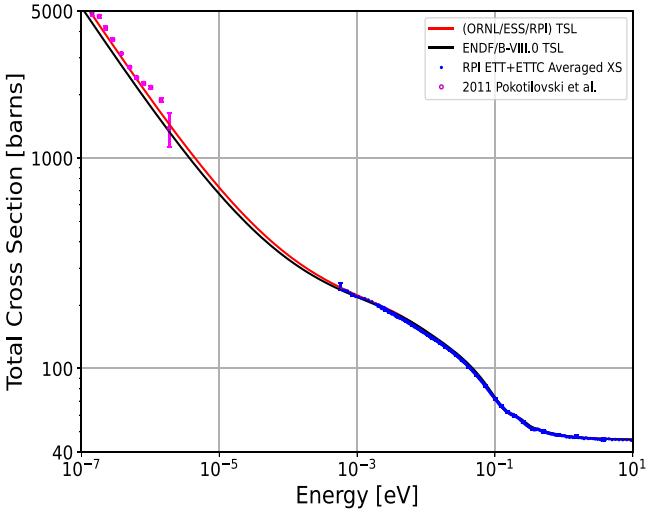

Fig. 9. Total cross section of high-density polyethylene from 0.1 μeV - 10 eV. Experimental error bars are plotted for all data points shown, but are hard to see due to their small magnitude. TSL evaluation processing performed with NCrystal due to 1e-5 eV processing cutoff in NJOY.

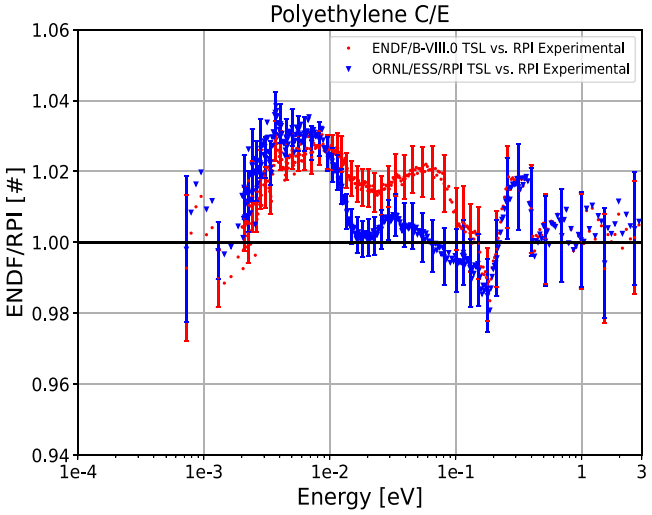

Fig. 8. Evaluation to RPI experiment ratio for the ENDF/B-VIII.0 and ORNL/ESS/RPI TSL evaluations for polyethylene. Error bars are not plotted for every point for plot visibility and represent the experimental uncertainty in the average polyethylene cross section.

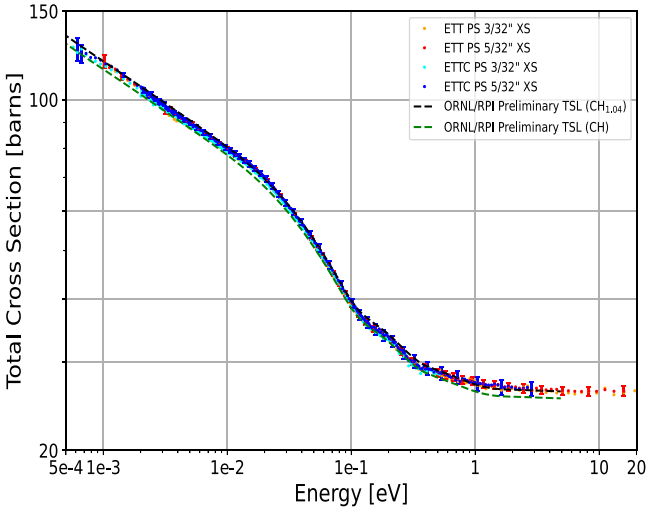

Fig. 10. Total cross section of polystyrene from 0.0005–20 eV.

in NJOY restricting processing to energies above 1e-5 eV. It should be noted that the processing of TSL evaluations below 1e-5 eV is beyond the normal range of applicability for general-purpose ENDF evaluations. While the evaluated data is not traditionally used below 1e-5 eV in most applications, validation of the total cross section at ultracold energies is still important as an integral quality check for the overall phonon spectra.

The total cross section for all of the polystyrene (PS) measurements are compared to a preliminary ORNL/RPI thermal scattering kernel evaluation below in Fig. 10. After experimentation, an elevated hydrogen concentration was found in the polystyrene samples that corresponded to $CH_{1.04}$ instead of CH, the simplified chemical formula for pure polystyrene. This elevated hydrogen concentration was later discovered to be due to a polystyrene–polybutadiene $[(C_{12}H_{14})_n]$ impurity present at an approximately 8% concentration. In order to understand the impact of this impurity on the molecular bond effects in polystyrene, a separate phonon spectrum was calculated using molecular dynamics in the same fashion for polystyrene–polybutadiene. The differences in the phonon spectra for polystyrene and polystyrene–polybutadiene were found to be negligible. Therefore, the preliminary ORNL/RPI polystyrene TSL evaluation was used for both the polystyrene and polystyrene–polybutadiene components. Fig. 10 shows the preliminary ORNL/RPI TSL evaluation for polystyrene at H/C ratios of 1 and 1.04.

Overall, very good agreement is seen between the polystyrene measurements and the ORNL/RPI preliminary TSL evaluation, and between the four polystyrene measurements themselves, over all energies. A slight misalignment is present in the cross section fluctuation around 0.2 eV between the preliminary evaluation and the measurements. It should be noted that experimental error bars are plotted for the two PS 5/32" measurements and represent the diagonal of the calculated covariance matrix. These total cross section measurements represent the first for polystyrene that encompass the entire thermal region.

Due to the excellent agreement between the four RPI measurements for polystyrene, the same cross section averaging method found in Danon et al. (2009) could also be applied to the polystyrene measurements. This average cross section was then used to create a C/E plot in a similar fashion to the polyethylene experimental data. This

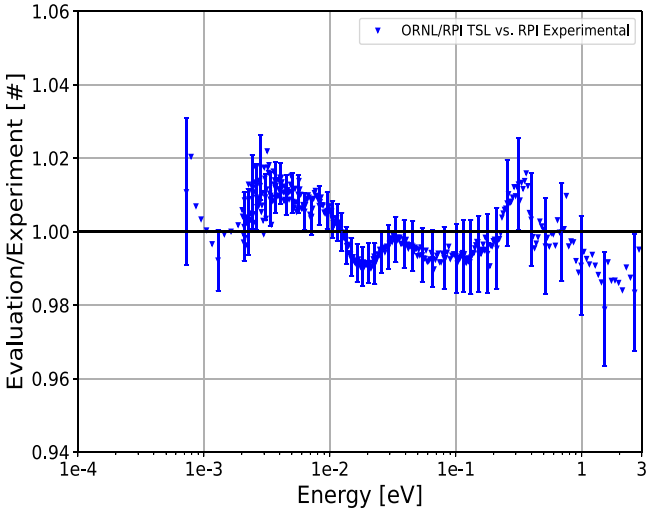

Fig. 11. Evaluation to RPI experiment ratio for the ORNL/RPI preliminary TSL evaluation for polystyrene at a H/C ratio of 1.04. Error bars are not plotted for every point for plot visibility and represent the experimental uncertainty in the average polystyrene cross section.

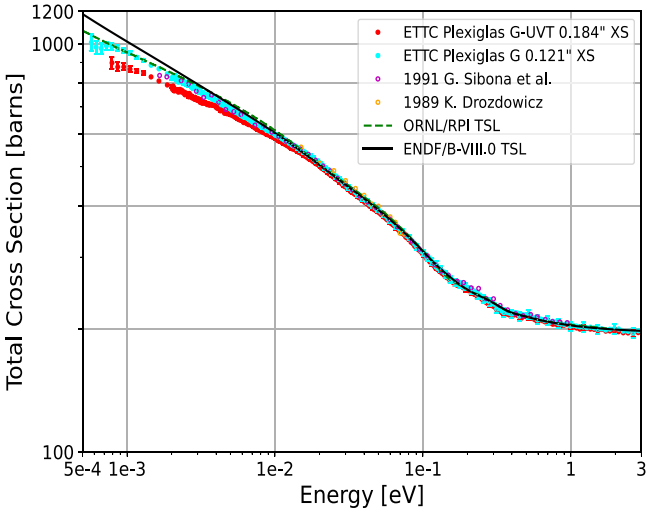

Fig. 12. Total cross section of Plexiglas G and Plexiglas G-UVT from 0.0005–3 eV.

C/E plot is shown in Fig. 11 and highlights the differences between the RPI measurements and the ORNL/RPI preliminary TSL evaluation for polystyrene. For the vast majority of data points the ORNL/RPI preliminary TSL evaluation for polystyrene agrees with the experimental data within 2%.

The total cross section for the Plexiglas G and Plexiglas G-UVT measurements are compared with the ENDF/B-VIII.0 and ORNL/RPI TSL evaluations, as well as experimental data from Drozdowicz (1989) and Sibona (1991) below in Fig. 12. It should be noted that in both the Drozdowicz and Sibona measurements, a generic 'plexiglass acrylic' material was used. In general, good agreement is seen between the Plexiglas G measurement and the experiments by Sibona and Drozdowicz.

When comparing the Plexiglas G and Plexiglas G-UVT measurements, good agreement is seen at energies above 0.02 eV. However, below 0.02 eV, the two measurements begin to diverge, with the difference in cross section increasing as the energy decreases. This discrepancy is not caused by a neutron absorber present in either material due to the elemental analysis performed. Instead, an Octadecanoic acid $[(CH_3(CH_2)_{16}COOH)_n]$ additive present in small, but unknown, quantities in Plexiglas G (Anon, 2021) (but not present in Plexiglas G-UVT) likely alters the molecular bond effects of the material and thereby distorts the neutron scattering cross section structure. For this reason, Plexiglas G-UVT represents a more pure form of Plexiglas acrylic, while Plexiglas G represents a more widely used form of Plexiglas acrylic. It should be noted that despite this additive, Plexiglas G and Plexiglas G-UVT have nearly identical thermo-physical properties with the exception of transparency to UV light. In addition, while Plexiglas G and Plexiglas G-UVT are trademarked forms of 'plexiglass', the small amount of Octadecanoic acid additive present in the Plexiglas G material does vary between manufacturers and can therefore result in small changes in the measured cross section for Plexiglas G.

The sensitivity of neutrons to molecular bond effects increases in general as the neutron energy decreases. When comparing the two measurements to the ENDF/B-VIII.0 evaluation, good agreement is seen above 0.02 eV, with a divergence from the measured cross section below this energy point. For perspective, the ENDF/B-VIII.0 evaluated cross section is approximately 5% and 13% larger than the Plexiglas G and Plexiglas G-UVT measurements, respectively, around 0.001 eV. Below 0.02 eV, the ORNL/RPI evaluation agrees well with the Plexiglas G sample. Both the ENDF/B-VIII.0 and ORNL/RPI evaluations are slightly misaligned in the cross section fluctuation around 0.2 eV.

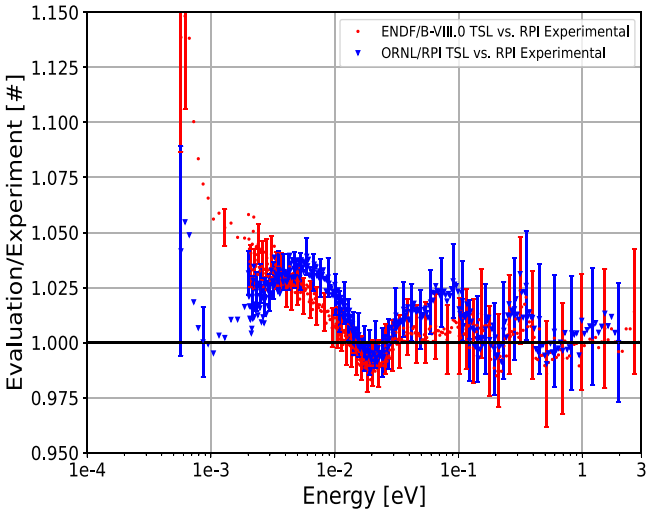

Fig. 13. Evaluation to RPI experiment ratio for the ENDF/B-VIII.0 and ORNL/RPI TSL evaluations for Plexiglas G. For both the ENDF/BVIII.0 and ORNL/RPI TSL evaluations, their discrepancy with the experiment is less than 5% for most energy points. Error bars are not plotted for every point for plot visibility and represent the experimental uncertainty in the Plexiglas G measurement.

Fig. 13 shows the C/E plot comparing the two TSL evaluations for Plexiglas directly to the Plexiglas G measurement. Above 0.003 eV, both TSL evaluations agree with the experimental data within 5%. However, below 0.003 eV the ENDF/B-VIII.0 TSL evaluation for Plexiglas strongly diverges from the Plexiglas G measurement as also seen in Fig. 12.

For all of the polymer materials, misalignments between experimental data and evaluations were present in the cross section fluctuations from 0.1–0.5 eV. These misalignments are most clearly visible in the C/E plots for each respective material in the form of a peak around 0.3 eV. While these peaks only represent a 2% deviation from the experimental cross section for each material, they suggest that there may be a systematic issue in how the phonon spectra for polymers are processed in NJOY.

6. Conclusions

Using a well known flight path at the RPI LINAC, four measurements were performed for polyethylene and polystyrene each from

0.0005–20 eV. Generally good agreement was found for polyethylene between the RPI measurements, the ENDF/B-VIII.0 evaluation, the ORNL/ESS/RPI evaluation and other experiments. However, some minor discrepancies were present at energies below 0.5 eV. For polystyrene, these measurements represent the first total cross section measurements to encompass the entire thermal energy range. Comparisons were made to a preliminary ORNL/RPI TSL evaluation, where good agreement was seen for a first attempt evaluation. However, some minor discrepancies were present in the 0.1–0.3 eV energy range.

Plexiglas G and Plexiglas G-UVT were measured from 0.0005–3 eV, representing the first measurements to have a well known sample material and encompassing a wider energy range than previous measurements. Generally good agreement was found for Plexiglas between the RPI measurements, the ENDF/B-VIII.0 and ORNL/RPI evaluations, as well as other experiments at energies above 0.02 eV. However, below 0.02 eV a divergence of cross section was found between the ENDF/B-VIII.0 evaluation, the Plexiglas G sample and the Plexiglas G-UVT sample, while the ORNL/RPI evaluation agreed with the Plexiglas G sample. Between the Plexiglas G and Plexiglas G-UVT samples, this divergence is very likely caused by a disruption to the molecular bond effects on neutron scattering cross section structure stemming from an additive present in Plexiglas G. Therefore, special care must be taken in identifying which Plexiglas material is used in critical experiments and for the creation of TSL evaluations. These measurements allowed for extensive collaboration between evaluators and experimentalists that resulted in significant improvements to the accuracy of TSL evaluations available for polymer materials.

Declaration of competing interest

The authors declare that they have no known competing financial interests or personal relationships that could have appeared to influence the work reported in this paper.

Data availability

Data for total cross section will be available in EXFOR.

Acknowledgments

The authors would like to thank Oak Ridge National Laboratory for providing the preliminary polystyrene TSL evaluation. In addition, thanks goes out to the RPI LINAC technical staff for their assistance in conducting these measurements. This work was supported by the Nuclear Criticality Safety Program, funded and managed by the National Nuclear Security Administration, USA for the Department of Energy. Additionally, this material is based upon work supported under an Integrated University Program Graduate Fellowship. Any opinions, findings, and conclusions or recommendations expressed in this publication are those of the author(s) and do not necessarily reflect the views of DOE.

References

Anon, 2021. Safety data sheet, Plexiglas G Colorless Acrylic Sheet. Altuglas LLC. Version 1.2. Issued on 06/07/2021.

Bess, J.D., Ivanova, T., Scott, L., Hill, I., 2019. The 2019 edition of the ICSBEP handbook. Trans. Am. Nucl. Soc. 121, 901–904. http://dx.doi.org/10.13182/T30703.

Brown, J.M., 2019. Measurements, Evaluation, and Validation of Ta-181 Resolved and Unresolved Resonance Regions (Submission for Doctor of Philosophy), Rensselear Polytechnic Institute.

Brown, D., Chadwick, M., Capote, R., Kahler, A., Trkov, A., Herman, W., Sonzogni, A., Danon, Y., Carlson, A., Dunn, M., Smith, D., Hale, G., Arbanas, G., Arcilla, R., Bates, C., Beck, B., Becker, B., Brown, F., Casperson, R., Conlin, J., Cullen, D., Descalle, M., Firestone, R., Gaines, T., Guber, K., Hawari, A., Holmes, J., Johnson, T., Kawano, T., Kiedrowski, C., Koning, A., Kopecky, S., Leal, L., Lestone, J., Lubitz, C., Marquez, J., Mattoon, C., McCutchan, E., Mughabghab, S., Navratil, P., Neudecker, D., Nobre, G., Noguere, G., Paris, M., Pigmi, M., Plompen, A., Pritychenko, B., Pronyaev, V., Roubtsov, D., Rochman, D., Romano, P., Schillebeeckx, P., Simakov, S., Sin, M., Sirakov, I., Sleaford, B., Sobes, V., Soukhovitskii, S., Stetcu, I., Talou, P., Thompson, I., van der Marck, S., Welser-Sherrill, S., Wiarda, D., White, M., Wormald, J., Wright, R., Zerkle, M., Aerovnik, G., Zhu, Y., 2018. ENDF/B-VIII.0: The 8th major release of the nuclear reaction data library with CIELO-project cross sections, new standards and thermal scattering data. Nucl. Data Sheets 148, 1–142.

Cai, X., Kittlemann, T., 2020. NCrystal: A library for thermal neutron transport. Comput. Phys. Commun. 246.

Cheng, Y.Q., Ramirez-Cuesta, A.J., 2020. Calculation of the thermal neutron scattering cross-section of solids using OCLIMAX. J. Chem. Theory Comput. 16 (8), 5212–5217. http://dx.doi.org/10.1021/acs.jctc.0c00569.

Danon, Y., 1993. Design and Contruction of the RPI Enhanced Thermal Neutron Target and Thermal Cross Section Measurements of Rare Earth Isotopes (Submission for Doctor of Philosophy). Rensselear Polytechnic Institute..

Danon, Y., Block, R., Rapp, M., Saglime, F., Leinweber, G., Barry, D., Drindak, N., Hoole, J., 2009. Beryllium and graphite high-accuracy total cross-section measurements in the energy range from 24 to 900 keV. Nucl. Sci. Eng. 161, 321–330.

de Laeter, J.R., Böhlke, J.K., Bièvre, P.D., Hidaka, H., Peiser, H.S., Rosman, K.J.R., Taylor, P.D.P., 2003. Atomic weights of the elements: Review 2000. Pure Appl. Chem. 75, 683–800.

Drozdowicz, K., 1989. Total cross section of plexiglass in the thermal neutron region. Ann. Nucl. Energy 16 (6), 275–278. http://dx.doi.org/10.1016/0306-4549(89)90130-8.

Fritz, D., Danon, Y., 2021. Enhancement of sub-thermal neutron flux through cold polyethylene. J. Neutron Res. 23 (2–3), 179–184. http://dx.doi.org/10.3233/JNR-210010.

Fritz, D., Danon, Y., 2022. Thermal neutron cross section measurements at the RPI LINAC. NCSP Technical Program Review, February.

Granada, J.R., Dawidowski, J., Mayer, R.E., Gillette, V.H., 1987. Thermal neutron cross section and transport properties of polyethylene. Nucl. Instrum. Methods Phys. Res. A 261, 573–578.

Lee, J., Nishiyama, J., Hori, J.-I., Kimura, R., Sako, T., Yamada, A., Sano, T., 2019. Neutron total cross section measurements of polyethylene using time-of-flight method at KURNS-LINAC. Nucl. Sci. Technol. 57, 1–8. http://dx.doi.org/10.1080/00223131.2019.1647894.

Macfarlane, R., Muir, D.W., Boicourt, R.M., Kahler, A.C., Conlin, J.L., 2017. The NJOY Nuclear Data Processing System, Version 2016. Tech. Rep., Los Alamos National Laboratory, LA-UR-17-20093.

Pokotilovski, Y., Novopoltsev, M., Geltenbort, P., Brenner, T., 2011. A differential time-of-flight spectrometer of very slow neutrons. Instrum. Exp. Tech. - Instrum Exp Tech-Engl TR 54, http://dx.doi.org/10.1134/S0020441210061077.

Ramic, K., Wendorff, C., Cheng, Y., Kolesnikov, A.I., Abernathy, D.L., Daemen, L., Arbanas, G., Leal, L., Danon, Y., Liu, L.E., 2018. Thermal scattering law of $(C_2H_4)_n$: Integrating experimental data with DFT calculations. Ann. Nucl. Energy 120, 778–787. http://dx.doi.org/10.1016/j.anucene.2018.06.029.

Ramic, K., Wendorff, C., Cheng, Y., Kolesnikov, A.I., Abernathy, D.L., Daemen, L., Arbanas, G., Leal, L., Danon, Y., Liu, L.E., 2019. Toward a better thermal scattering law of $(C_5O_2H_8)_n$: Inelastic neutron scattering and oClimax+NJOY2016. Ann. Nucl. Energy 133, 425–430. http://dx.doi.org/10.1016/j.anucene.2019.05.042.

Sibona, G., 1991. Thermal neutron cross sections and diffusion parameters of plexiglass. Ann. Nucl. Energy 18, 689–696. http://dx.doi.org/10.1016/0306-4549(91)90042-V.

Syme, D., 1982. The black and white-filter method for background determination in neutron time-of-flight spectrometry. Nucl. Instrum. Methods 198, 357–364.

Werner, C.J., Bull, J.S., Solomon, C.J., Brown, F.B., McKinney, G.W., Rising, M.E., Dixon, D.A., Martz, R.L., Hughes, H.G., Cox, L.J., Zukaitis, A.J., Armstrong, J.C., Forster, R.A., Casswell, L., 2018. MCNP-6.2 Release Notes, LA-UR-18-20808. Tech. Rep., Los Alamos National Laboratory, http://dx.doi.org/10.2172/1419730.

Zhu, Y., Hawari, A.I., 2018. FLASSH, full law analysis scattering system hub. In: Proceedings of PHYSOR 2018, Cancun, Mexico, April 22-26.